

Synthesis and Ionic Conductivity of Phosphate-Sulfate Fluorapatites $\text{Ca}_{10-x}\text{Na}_x(\text{PO}_4)_6-x(\text{SO}_4)_x\text{F}_2$ ($x = 0;3;6$)

faten nouri (✉ nourifeten@gmail.com)

FSB

riadh ternane

fsb

malika ayadi

fsb

Research Article

Keywords: Fluorapatite, Complex impedance, spectroscopy, Ionic conductivity, SOFC

Posted Date: June 11th, 2021

DOI: <https://doi.org/10.21203/rs.3.rs-607251/v1>

License:   This work is licensed under a Creative Commons Attribution 4.0 International License.

[Read Full License](#)

Abstract

Background

Solid-state electrolytes for Solid Oxide Fuel Cells (SOFC) with high ionic conductivities has attracted great interest for electrochemical applications because of their interesting ionic conduction.

Methods

Complex impedance spectroscopy (CIS) was used to study the electrical properties of Phosphate-sulfatefluorapatite.

Findings

Phosphate-sulfatefluorapatite $\text{Ca}_{10-x}\text{Na}_x(\text{PO}_4)_{6-x}(\text{SO}_4)_x\text{F}_2$ ($x = 0;3;6$), have been synthesized by the solid-state reaction at high temperature. The samples have been characterized by X-ray Diffraction (XRD), Fourier transform infrared spectroscopy (FTIR), Raman scattering spectroscopy, and Transmission Electron Microscopy (TEM) techniques. XRD study shows that these materials crystallize in the hexagonal system with $P6_3/m$ as a space group. An impedance analysis has been used to analyze the electrical behavior of the samples at different temperatures. Evidence of temperature-dependent electrical relaxation phenomena is observed. The bulk resistance decreases with increasing temperature, showing a typical negative temperature coefficient of resistance (NTCR). AC-conductivity measurements have been performed on a wide range of frequencies and temperatures. The ionic conductivity follows the Arrhenius and the Jonscher laws.

Introduction

In recent years, a wide variety of new solid electrolytes for Solid Oxide Fuel Cells (SOFC) with high ionic conductivities has attracted great interest for electrochemical applications. In these devices; the electrolyte must be an ionic conductor with negligible electronic contribution, and it must be dense to prevent gas mixing[1-5]. The anode and cathode should have good electronic or mixed conductivity, in addition to some catalytic activity towards fuel oxidation and oxygen reduction, respectively.

Apatites are solid inorganic compounds, represented by the general formula $\text{Me}_{10}(\text{XO}_4)_6\text{A}_2$, ($P6_3/m$ space group). The apatite structure provides a great capacity to form solid solutions and, particularly, to accept several substitutes[6,7-15]. The monovalent A ion can be OH^- , F^- , O^{2-} , CO_3^{2-} ..., the trivalent anion XO_4 can be AsO_4^{3-} , VO_4^{3-} , CrO_4^{3-} , SiO_4^{4-} , HPO_4^{2-} , CO_3^{2-} . There is no literature information showing that vacancies could exist on the (XO_4) site. Me cations may be divalent (Ca^{2+} , Ba^{2+} , Pb^{2+}) monovalent (Na^+). The apatite-like structure is characterized by the presence of two types of tunnels permitting the location of two cationic sites labeled Me(I) and Me(II): four Me(I) are at the center of narrow tunnels (4f sites), six Me(II) around large tunnels (6h sites). The A⁻anions are located on the hexad axis (2a

sites). The coordination number of Me (I) and Me(II) sites are nine and seven, respectively. However, extensive substitutions can occur on the different cation and anion sites in mineral samples.

Since the P-O and S-O bond distances in the corresponding PO_4^{3-} and SO_4^{2-} tetrahedral are similar (P-O: 1.50 Å, S-O: 1.44 Å) [16,17], up to now the group of sulfate apatite has not been studied in such details. Sulfate apatite is derived from phosphate apatite by coupled substitution of PO_4^{3-} and Ca^{2+} with SO_4^{2-} and Na^+ [18].

Complex impedance spectroscopy is a well-established method to investigate the electrical properties of materials. This technique offers enormous possibilities to investigate the electrical and electrochemical properties of materials, the study of relaxation phenomena, and the resolution of bulk, grain boundaries, and electrode-electrolyte interface contributions are often probed.

In recent years apatites, $\text{Me}_{10}(\text{XO}_4)_6\text{A}_2$ have been attracting considerable interest as solid electrolytes for SOFC. It can be related to the mobility of charges in the apatite network. The mobility of A ions that are the main charge carriers in apatitic materials for obtaining solid electrolytes can be mentioned [12-14, 19-23].

It is, therefore, necessary to develop scientific research on other types of synthetic apatites. In this work, $\text{Ca}_{10-x}\text{Na}_x(\text{PO}_4)_{6-x}(\text{SO}_4)_x\text{F}_2$ ($x = 0, 3, 6$) fluorapatite have been prepared by solid-state reaction. The structural characterization of these materials has been performed by XRD, FTIR, Raman, and TEM techniques. Ionic properties of this fluorapatite have been investigated by complex impedance spectroscopy.

Experimental

2.1. Synthesis

The $\text{Ca}_{10-x}\text{Na}_x(\text{PO}_4)_{6-x}(\text{SO}_4)_x\text{F}_2$ ($x = 0, 3, 6$) fluorapatite have been synthesized by solid-state reaction. The temperature was varied between 773 K, 823 K, and 1173 K depending on the sulfur to phosphorus atomic ratio (S/P). The pure phosphate apatite $\text{Ca}_{10}(\text{PO}_4)_6\text{F}_2$ ($x=0$) was obtained at a higher temperature (1173 K) than that of phosphate-sulfate apatite $\text{Ca}_7\text{Na}_3(\text{PO}_4)_3(\text{SO}_4)_3\text{F}_2$ ($x=3$) (823 K) and of pure sulfate apatite $\text{Ca}_4\text{Na}_6(\text{SO}_4)_6\text{F}_2$ ($x=6$) (773 K). The samples were prepared by an initial mixture of sodium sulfate Na_2SO_4 , calcium carbonate CaCO_3 , calcium fluoride CaF_2 , di-ammonium hydrogen phosphate $(\text{NH}_4)_2\text{HPO}_4$, and di-ammonium sulfate $(\text{NH}_4)_2\text{SO}_4$, with the Ca+Na/S+P atomic ratio fixed at 1.667. Stoichiometric amounts of reactants have been ground and heated in covered platinum crucibles at 773 K for 72h, then at 823 K for 24 h, and at 1173 K for 72h. The heat treatment was accompanied by several grindings to get well-crystallized products.

2.2. Experimental techniques

The XRD patterns were recorded with a Bruker D8-advance diffractometer using CuK α radiation ($\lambda = 1.54004 \text{ \AA}$). XRD data were collected over the 10-55° 2 θ range with a 0.021 step and at regular intervals of 12 s. The crystalline phases were identified using the International Center for Diffraction Data (ICDD) powder diffraction files. The cell parameters were calculated by using the program "FullProf".

TEM powder specimens were prepared by dispersing a small number of powders in ethanol under an ultrasonic bath for few minutes, followed by dropping the suspension onto a holey-carbon coated copper grid. HRTEM study was carried out in a JEOL JEM-3010 microscope operated under 300 kV.

Electrical conductivity measurements were obtained using a Hewlett-Packard HP 4192 analyzer as a function of temperature. The impedance measurements were taken in a circuit using two-electrode configurations with a signal amplitude of 50 mV and a frequency band ranging from 5 Hz to 13 MHz. High-temperature measurements were performed between 673 and 773 K under air atmosphere. Powders were pressed under 5 t. cm⁻² and sintered at 850 K. Both pellet surfaces were coated with silver paste electrodes while the platinum wires attached to the electrodes were used as current collectors. The Z-View software was used to analyze the impedance data in equivalent circuits.

The electrical conductivity values were deduced from the following equation:

$$\sigma = \frac{e}{R.S} \quad (1)$$

Where R is the resistance deduced from impedance diagrams and S and e are the area and the thickness of pellets, respectively.

The dependence of the conductivity can be described by the Arrhenius equation:

$$\sigma = A/T \exp(-E_{a\sigma}/kT) \quad (2)$$

Where A is a pre-exponential factor (which is related to the effective number of mobile species), k is the Boltzmann constant, E_{a σ} is the activation energy and T is the absolute temperature.

Results And Discussion

3.1. XRD

Fig.1 shows the XRD patterns of the synthesized samples Ca₁₀(PO₄)₆F₂(x=0), Ca₇Na₃(PO₄)₃(SO₄)₃F₂(x=3) and Ca₄Na₆(SO₄)₆F₂(x=6). The results confirm that the samples are formed by an apatitic phase; all the lines are indexed in the hexagonal system (space group P6₃/m). The unit-cell parameter values of these compounds are reported in Table 1.

The purity of the compounds is then confirmed by the IR absorption spectroscopy and Raman scattering spectroscopy [24].

3.2. TEM

TEM micrograph of phosphate fluorapatite $\text{Ca}_{10}(\text{PO}_4)_6\text{F}_2$ ($x=0$) shows that the particles are of spheroid geometry Fig.2 . However, the incorporation of SO_4^{2-} ions influenced the shape of the particles. The morphology of the grains seems to be similar and has a rather irregular shape with the formation of agglomerates of different sizes.

The EDS (Energie Dispersive Spectroscopy) spectra Fig.3 show the presence of Ca, Na, S, P, O, and F elements constituting the synthesized fluorapatite. This confirms the successful incorporation of SO_4^{2-} and PO_4^{3-} ions into the lattice through the increased intensity of elemental phosphorus and sulfur. Small intensity peaks due to Na are observed, leading to Na substitution.

3.3 Ionic conductivity

3.3.1. Complex electrical impedance analysis

The impedance spectroscopy (IS) is a powerful non-destructive technique for the characterization of the electrical behavior of materials.

Fig.4. shows typical complex impedance spectra (Nyquist plots) of $\text{Ca}_7\text{Na}_3(\text{PO}_4)_3(\text{SO}_4)_3\text{F}_2$ ($x=3$) fluorapatite, over a wide range of temperatures [673-773 K]. The impedance spectrum is characterized by the appearance of a single semicircular arc whose radius of curvature decreases as temperature increases. This can be attributed to the presence of electrical relaxation phenomena in the materials under investigation [25]. The effect of temperature on impedance behavior is much notable at higher temperatures.

The intercept of the semicircular arc with the real axis gives an estimate of sample resistance. The resistance decreases and conductivity increases with temperature indicating an activated conduction mechanism Table.2. This behavior is analogous to the negative temperature coefficient of resistance (NTCR) property reported in semi-conductors.

3.3.2 ac-Conductivity

The study of the ion transport properties of the materials is necessarily carried out with the measurements of the ac-conductivity. Processes take place with the passage of an alternating electric current through the solid electrolyte such as ionic movement through the electrolyte mass, charge transfer through the electrode-electrolyte interface, occurs.

The dependence of the ac-conductivity (σ_{ac}) with frequency at different temperatures of $\text{Ca}_7\text{Na}_3(\text{PO}_4)_3(\text{SO}_4)_3\text{F}_2$ is illustrated in Fig.5. The curves clearly show two distinctly frequency regions which can be separated by a change in the slope for each temperature. The "hopping frequency", denoted (ω_p), is at which the frequency of the ac conductivity changes. It is important to note that the evolution

of $\omega\rho$ is proportional to the temperature, so it increases with the temperature. Fig.5 shows that σ_{ac} decreases with decreasing frequency and becomes independent of frequency after a certain value. At higher frequencies, the values of ac electrical conductivity become closer, and are temperature-independent.

Globally, the ac conductivity behavior in all temperature ranges is well described by Jonscher's universal power law [26-28] governed by the relation:

$$\sigma_{ac}(\omega) = \sigma_{dc} + B \omega^n (0 < n < 1) \quad (3)$$

Where σ_{dc} is the dc conductivity, which is calculated by extrapolation of the curves of σ_{ac} to zero frequency for different temperatures.

In the higher frequency domain, conductivity increases linearly with frequency for all samples, whereas at low frequencies it is almost independent with frequency, which could be assigned to dc contribution (σ_{dc}).

The behavior of the conductivity at high frequency obeys the following law: $\sigma_{ac} = B\omega^n$

The exponent, n , depends on the degree of ion-ion interaction existing in the ionic hopping process. The ac conductivity (σ_{ac}) measurements have been widely used to investigate the nature of defect centers in disordered systems since it is assumed that they are responsible for this type of conduction. The exponent, n , would equal zero in the case of independent random ion hopping (absence of interactions) whereas it would tend towards 1 for a complete correlation ion motion [29-30]. The value of the exponent, n , for every compound studied in this work is calculated by fitting the frequency dependence of the isothermal conductivity data to the above-mentioned extended Jonscher-type expression for a selected temperature.

At higher frequencies, σ_{ac} shows frequency dependence that gives rise to ac-conductivity. In this case, σ_{ac} increases roughly in a power-law fashion; $\sigma_{ac}(\omega) = B\omega^n$ and eventually becomes almost linear at even higher temperatures.

Fig.6 shows the $\ln(\sigma T)$ versus $1000/T$ plot of the $\text{Ca}_{10-x}\text{Na}_x(\text{PO}_4)_{6-x}(\text{SO}_4)_x\text{F}_2$ ($x=0, 3, 6$) fluorapatite. It should be noted that, in the studied temperature range, the conductivity of the fluorapatite, verifies the Arrhenius law relative to a diffusion mechanism and that the materials exhibit a semiconductor behavior since the conductivity increases.

From the slope plot that activation energy values, $E_{a\sigma}$, can be calculated. The conductivity (σ) values at 773 K and activation energies $E_{a\sigma}$ are illustrated in Table 3. Ionic conductivity and activation energy can be related to those of F^- and Na^+ ions, then move to other positions by the formation of thermally activated Schottky defects. Thus, detected conductivity is ascribed to F^- and Na^+ mobility, largely dependent on the chemical disorder detected in apatites.

Fig.7. shows the variation in the activation energy as a function of the sulfur content. A maximum conductivity appears for the $\text{Ca}_7\text{Na}_3(\text{PO}_4)_3(\text{SO}_4)_3\text{F}_2$ ($x = 3$) apatite Table3. This maximum corresponds to the lowest activation energy.

The frequency dependence of the imaginary part of impedance ($-Z''$) of $\text{Ca}_7\text{Na}_3(\text{PO}_4)_3(\text{SO}_4)_3\text{F}_2(x = 3)$ at different temperatures is shown in Fig.8.

The peak shifts to higher frequencies with the increase in temperature. It indicates a thermally activated dielectric relaxation process and shows a progressive decrease in the bulk resistance when temperature increases. That might be down to the accumulation of ions at higher temperatures. The significant asymmetric broadening of peaks with rising temperatures suggests the presence of a temperature-dependent relaxation process. This behavior is due to the presence of space charge polarization at lower frequencies disappearing at higher frequencies [31].

Indeed, at higher temperatures, the peak height representing the relaxation shows a progressive increment with S content.

The impedance data are used to evaluate the relaxation time (τ) of the electrical phenomena in the material using the relation:

$$\tau = \frac{1}{2\pi f_{max}} = RC \quad (4)$$

Where τ is the relaxation time expressed by:

$$\tau = \tau_0 \exp \left(\frac{E_{a\tau}}{KT} \right) \quad (5)$$

Where τ_0 is the pre-exponential factor, $E_{a\tau}$ is the activation energy of the relaxation phenomena, K is the Boltzmann constant and T is the absolute temperature.

The variation of τ with temperature is shown in Fig.9. These plots show a steady increase in the relaxation time with rising temperature. This result suggests the presence of temperature-dependent electrical relaxation phenomena in the material, possibly due to the migration of species/defects. Activation energies ($E_{a\tau}$) deduced from the slope of the $\ln(\tau)$ against $1000/T$ curve are close to that of the activation energy ($E_{a\sigma}$) Table 3.

Conclusion

Fluorapatites $\text{Ca}_{10-x}\text{Na}_x(\text{PO}_4)_{6-x}(\text{SO}_4)_x\text{F}_2$ ($x=0, 3, 6$) have been synthesized by the solid-state reaction at high temperature. XRD and TEM techniques have confirmed the formation of single apatite phases.

The analysis of the electrical properties shows that prepared apatites exhibit negative temperature coefficient of resistances (NTCR) and temperature-dependent relaxation phenomena. The complex impedance analysis suggests the presence of non-Debye relaxations that would be associated with correlation on ions motion. The ionic conductivity follows the Arrhenius and the Jonscher laws.

References

1. Hosseini SM, Shvareva T, Navrotsky A, Energetics of lanthanum silicate apatite: Influence of interstitial oxygen and cation vacancy concentrations in $\text{La}_{9.33+x}(\text{SiO}_4)_6\text{O}_{2+3x/2}$ and $\text{La}_{10-x}\text{Sr}_x(\text{SiO}_4)_6\text{O}_{3-0.5x}$. *Solid State Ionics*. 2013; 233:62–66
2. Santos M, Alves C, Oliveira FAC, Marcelo T, Mascarenhas J, Cavaleiro A (2013) B Trindade, Novel two-step processing route combining mechanical alloying and microwave hybrid sintering to fabricate dense $\text{La}_{9.33}\text{Si}_2\text{Ge}_4\text{O}_{26}$ for SOFCs. *J Power Sources* 231:146–152
3. Orera A, Baikie T, Kendrick E, Shin JF, Pramana S, Smith R, White TJ, Sanjuan ML, Slater PR (2011) Apatite germanates doped with tungsten: synthesis, structure, and conductivity. *Dalton Trans* 40:3903–3908
4. Sun F, Zhang NN, Li JL, Liao HL (2013) Preparation of dense silicate electrolyte coating with low pressure plasma spraying and very low pressure plasma spraying for intermediate-temperature solid oxide fuel cells. *J Power Sources* 223:36–41
5. Nakayama S, Ikesue A, Higuchi Y, Sugawara M, Sakamoto M (2013) Growth of single-crystals of apatite-type oxide ionic conductor from sintered ceramics by a seeding method. *J Eur Ceram Soc* 33:207–210
6. Prener JS (1971) Nonstoichiometry in calcium chlorapatite. *J Solid State Chem* 3:49–55
7. Leon-Reina L, Martin-Sedeno MC, Losilla ER, Cabeza A, Martinez-Lara M, Brusque S, Marques FMB, Sheptyakov DV (2003) Aranda M A G, Crystal chemistry and oxide ion conductivity in the lanthanum oxygermanate apatite series. *Chem Mater* 15:2099–2108
8. Guillot S, Beaudet-Savignat S, Lambert S, Vannier RN, Roussel P, Porcher F
9. Evidence of local defects (2009) in the oxygen excess apatite $\text{La}_{9.67}(\text{SiO}_4)_6\text{O}_{2.5}$ from high resolution neutron powder diffraction. *J Solid State Chem* 182:3358–3364
10. Beaudet-Savignat S, Vincent A, Lambert S, Gervais F, Oxide ion conduction in Ba, Ca and Sr doped apatite-type lanthanum silicates. *J Mater Chem* 2007;17:2078–2087
11. Okudera H, Masubuchi Y, Kikkaw S (2005) Yoshiasa A, Structure of oxide ion-conducting lanthanum oxyapatite $\text{La}_{9.33}(\text{SiO}_4)_6\text{O}_2$. *Solid State Ionics* 176:1473–1478
12. Sansom JEH, Tolchard JR, Slater PR, Islam MS (2004) Synthesis and structural characterisation of the apatite-type phases $\text{La}_{10-x}\text{Si}_6\text{O}_{26+z}$ doped with Ga. *Solid State Ionics* 167:17–22
13. Chakroun E, Ternane R, Ben Hassen-Chehimi D, Trabelsi-Ayadi M (2008) Synthesis, characterization and electrical properties of a lead sodium vanadate apatite. *Mat Res Bull* 43:2451–2456

14. Abbassi M, Ternane R, Sobrados I, Madani A, Trabelsi-Ayadi M, Sanz J (2013) Ionic conductivity of apatite-type solid electrolyte ceramics $\text{Ca}_{2-x}\text{Ba}_x\text{La}_4\text{Bi}_4(\text{SiO}_4)_6\text{O}_2$ ($0 \leq x \leq 2$). *Ceram Int* 39:9215–9221
15. Abbassi M, Ternane R, Sobrados I, Madani A, Trabelsi-Ayadi M, Sanz J (2014) Synthesis, characterization and oxide conduction in Ba doped apatite-type silicates $\text{Ca}_2\text{La}_6\text{Bi}_2(\text{SiO}_4)_6\text{O}_2$. *Mater Chem Phys* 147:285–292
16. Nouri F, Panczer G, Guyot Y, Trabelsi-Ayadi M, Ternane R (2017) Synthesis and luminescent properties of Eu^{3+} -doped phosphate-sulfate fluorapatites $\text{Ca}_{10-x}\text{Na}_x(\text{PO}_4)_{6-x}(\text{SO}_4)_x\text{F}_2$. *J Lumin* 192:590–594
17. Prince E (2004) *J Int T Crystallogr* 200:;32
18. Botta C, Kahlenberg V, Hejny C, Többens DM, Bykov M, Van Smaalen S
19. *Miner P* 2014;108;487–501
20. Klement R, Natrium-calcium-sulfatapatite $\text{Na}_6\text{Ca}_4(\text{SO}_4)_6\text{F}_2$, *Natur wissenschaften*, 1939;27;568–568
21. Laghzizil A, El Hajjaji S, Bouhaouss A, Ferhat M (1999) Ionic conductivities of lithium fluorapatites. *Solid State Ionics* 126:245–250
22. Laghzizil A, Bouhaouss A, Barboux P, Morineau R, Livage J (1993) Mixed ionic conductivities in sodium fluoroapatites. *Solid State Ionics* 67:137–143
23. Piotrowski A, Kahlenberg V, Fischer RX (2004) Mixed phosphate-sulfate fluorapatites: possible materials in dental fillers. *Eur J Mineral* 16:279–284
24. Tazzoli V (1983) The crystal structure of cesanite, $\text{Ca}_{1+x}\text{Na}_{4-x}(\text{SO}_4)_3(\text{OH})_x(1-x)\text{H}_2\text{O}$. *Mineral Mag* 47:59–63
25. Piotrowski A, Kahlenberg V, Fischer RX, Lee Y, Parise JB (2002) The crystal structure of cesanite and its synthetic analogue- a comparison. *Am Mineral* 87:715–720
26. Nouri F, Panczer G, Trabelsi-Ayadi M, Ternane R, Synthesis and vibrational study of phosphate-sulfate fluorapatites $\text{Ca}_{10-x}\text{Na}_x(\text{PO}_4)_{6-x}(\text{SO}_4)_x\text{F}_2$ ($0 \leq x \leq 6$), *J Adv Chem* 2016; 12;4975–4980
27. Molak A, Paluch M, Pawlus S, Klimontko J, Ujma Z, Gruszka I (2005) Electric modulus approach to the analysis of electric relaxation in highly conducting $(\text{Na}_{0.75}\text{Bi}_{0.25})(\text{Mn}_{0.25}\text{Nb}_{0.75})\text{O}_3$. *J Phys* 38:1450–1460
28. Jonscher AK (1983) *Dielectric Relaxation in Solids*. Chelsea Dielectric Press
29. Jonscher AK (1977) The ‘universal’ dielectric response. *Nature* 267:673–679
30. Jonscher AK, A new understanding of the dielectric relaxation of solids. *J Mater Sci* 1981;16;2037–2060
31. Maiti GC, Freund F (1981) Influence of fluorine substitution on the proton conductivity of hydroxyapatite. *J Chem Soc Dalton Trans* 12:949–955
32. Funke K (1994) Jump relaxation model and coupling model- a comparison. *J Non-Cryst Solids* 172–174:;1215–1221

33. Ngai KL, Tsang KY (1999) Similarity of relaxation in super cooled liquids and interacting arrays of oscillators. Phys Rev E 60:4511–4517

Tables

Table1

Unit-cell parameters of the $\text{Ca}_{10-x}\text{Na}_x(\text{PO}_4)_{6-x}(\text{SO}_4)_x\text{F}_2$ fluorapatites.

S content (x)	0	3	6
a(Å)	9.381(1)	9.360(7)	9.340(6)
c(Å)	6.875(3)	6.864(6)	6.853(0)
Crystal system	Hexagonal		
Space group	P6 ₃ /m		

Table2

Resistances and conductivities of $\text{Ca}_7\text{Na}_3(\text{PO}_4)_3(\text{SO}_4)_3\text{F}_2$ (x = 3) fluorapatite at different temperatures.

T(K)	R(Ω)	σ (10^{-5} S.cm ⁻¹)
673	10748	0.493
693	3680.7	1.439
713	2348.9	2.256
733	1413.8	3.748
773	894.63	5.924

Table3

Resistances, conductivities and activation energies of $\text{Ca}_{10-x}\text{Na}_x(\text{PO}_4)_{6-x}(\text{SO}_4)_x\text{F}_2$ fluorapatites.

S content (x)	R(Ω) at 773 K	σ (S. cm ⁻¹) at 773 K	E _{aσ} (eV)	E _{aτ} (eV)
0	1.328 10 ⁶	0.654 10 ⁻⁷	1.67	1.64
3	894.63	0.592 10 ⁻⁴	0.97	0.95
6	22160	0.282 10 ⁻⁵	1	1.1

Figures

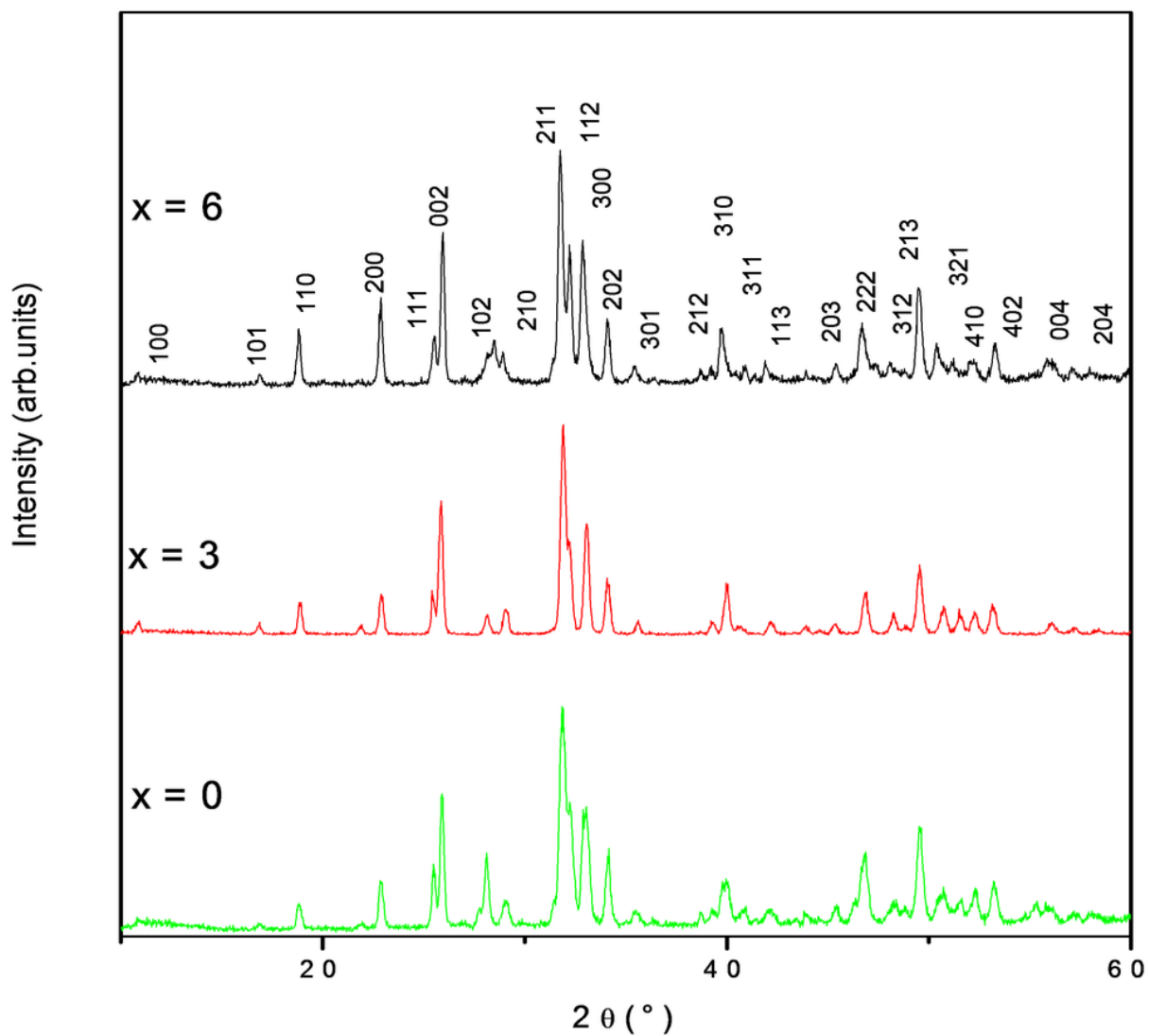


Figure 1

XRD patterns of $\text{Ca}_{10-x}\text{Na}_x(\text{PO}_4)_6-x(\text{SO}_4)_x\text{F}_2$ fluorapatites.

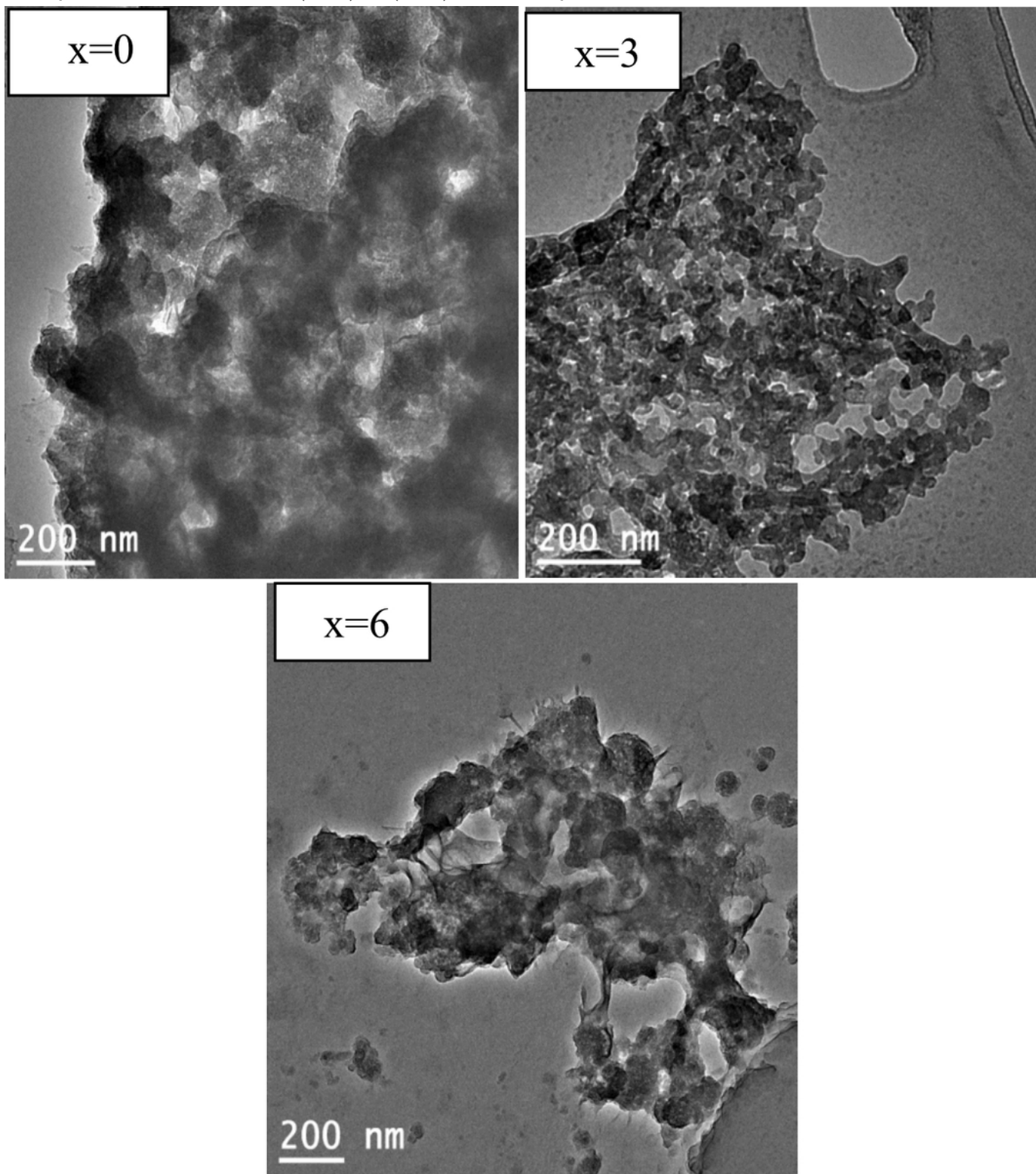


Figure 2

TEM micrographs of $\text{Ca}_{10-x}\text{Na}_x(\text{PO}_4)_6-x(\text{SO}_4)_x\text{F}_2$ fluorapatites

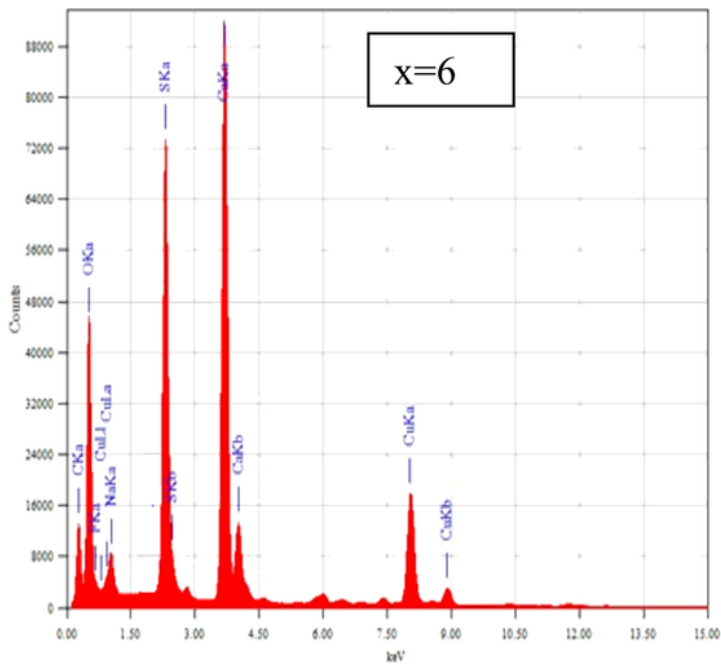
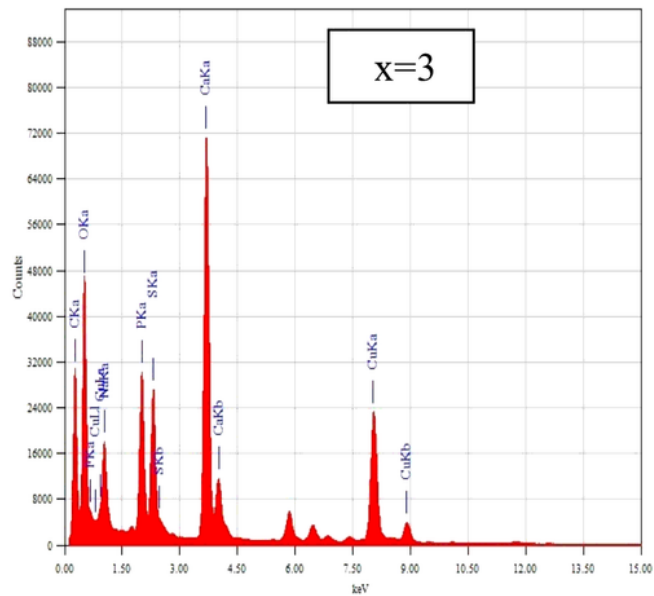
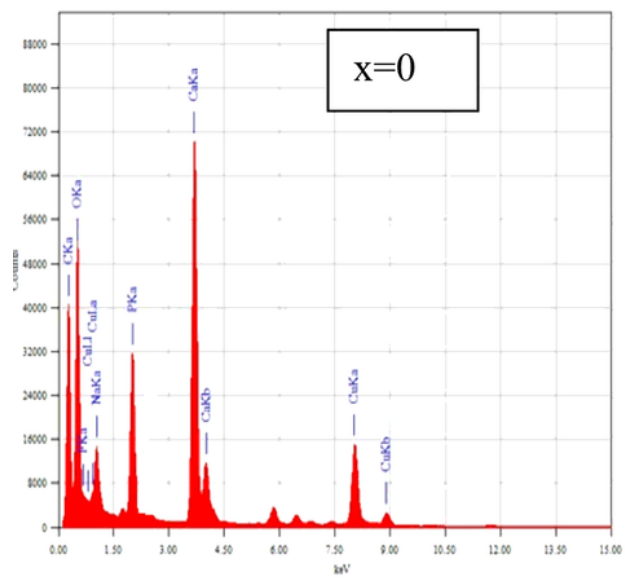


Figure 3

EDS spectra of $\text{Ca}_{10-x}\text{Na}_x(\text{PO}_4)_6-x(\text{SO}_4)_x\text{F}_2$ fluorapatites.

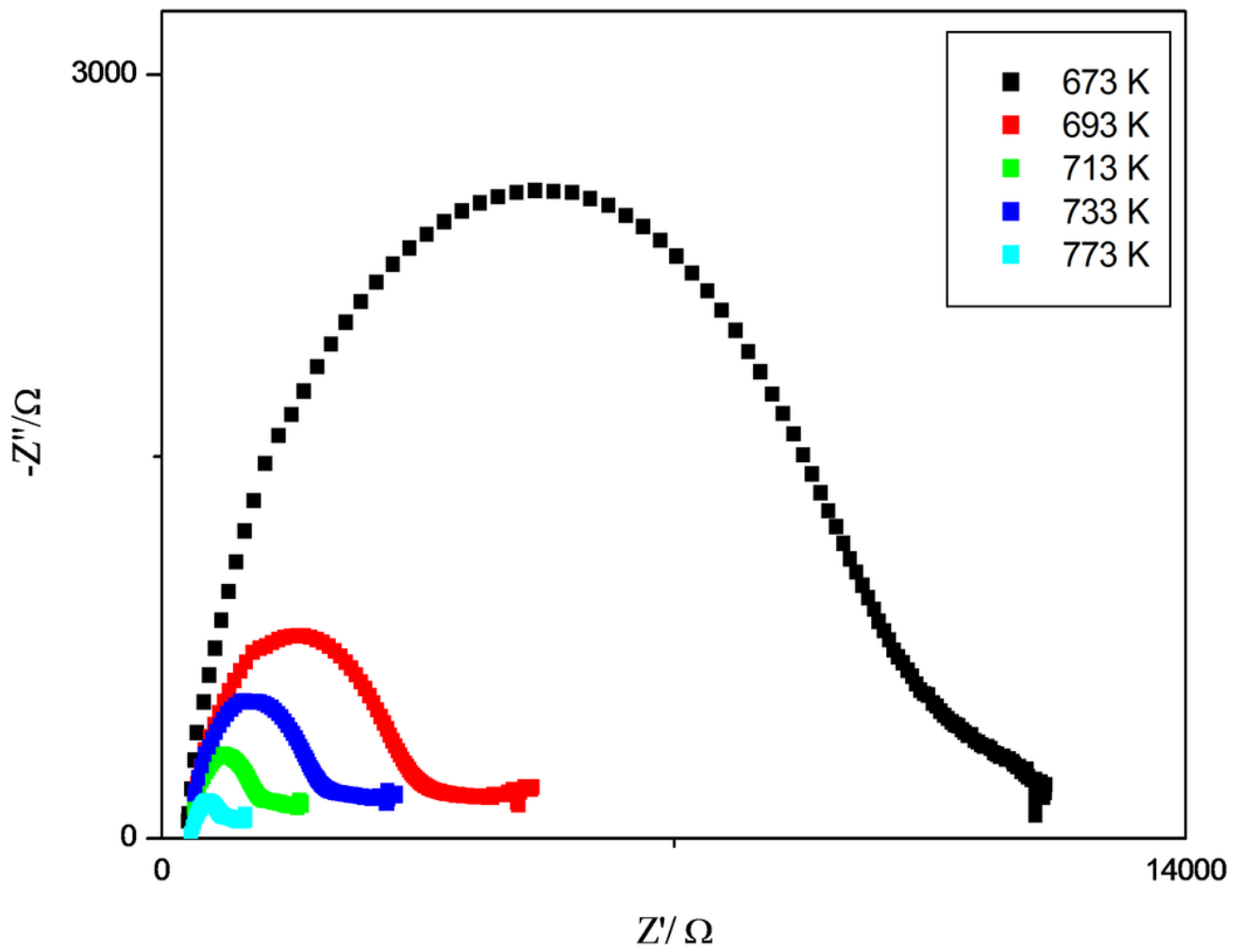


Figure 4

Nyquist diagrams ($-Z''$ versus Z') of Ca₇Na₃(P₀₄)₃(SO₄)₃F₂ (x=3) fluorapatite.

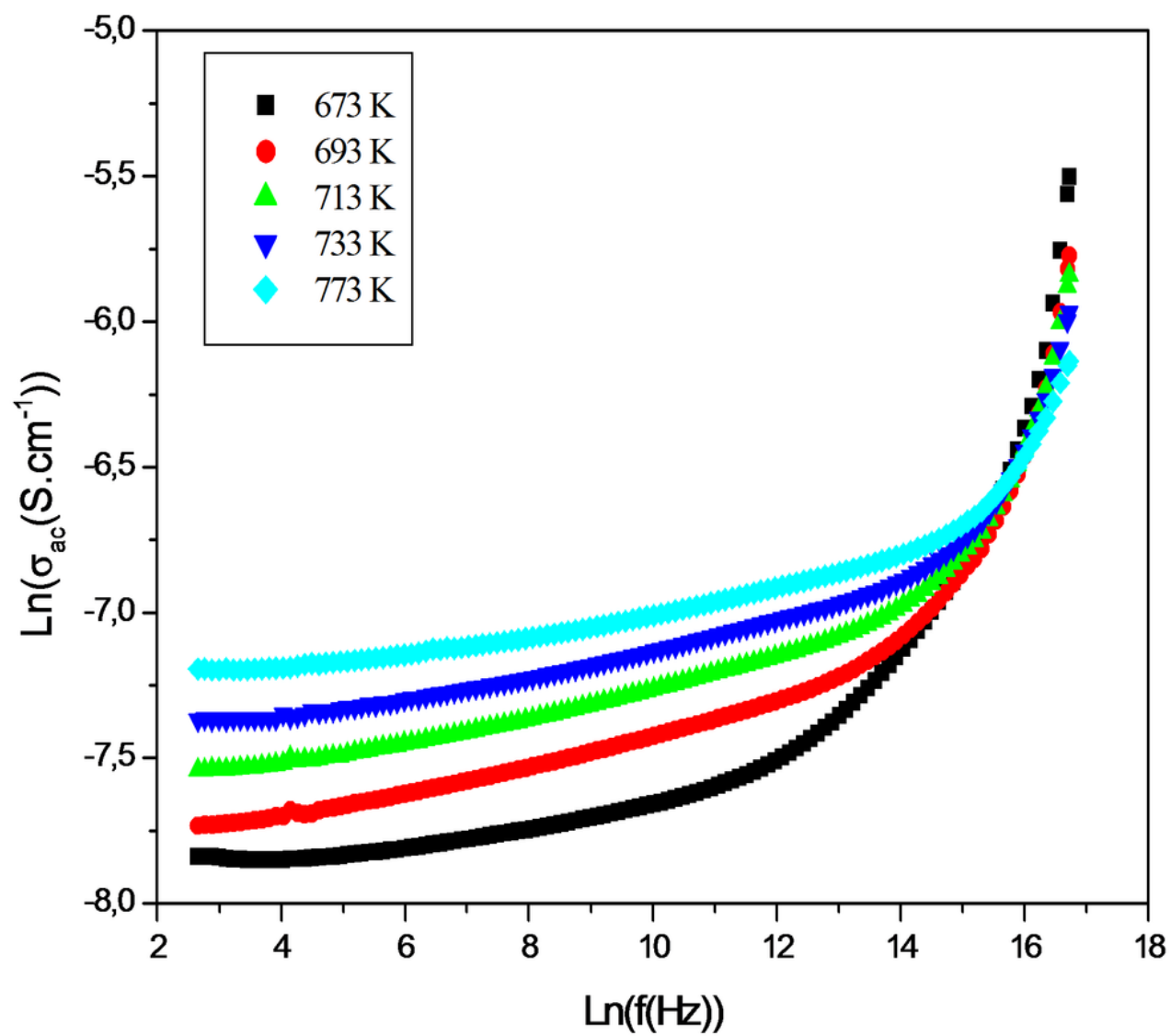


Figure 5

Frequency dependence of ac- conductivity at different temperatures of $\text{Ca}_7\text{Na}_3(\text{PO}_4)_3(\text{SO}_4)_3\text{F}_2(x=3)$ fluorapatite.

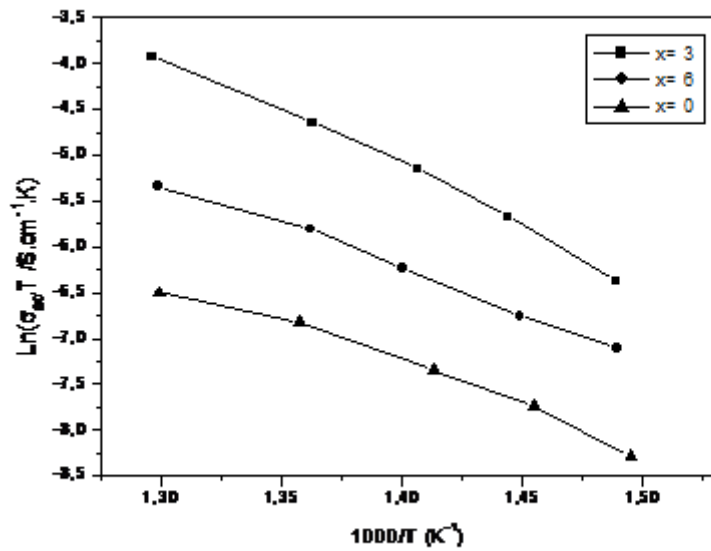


Figure 6

Arrhenius plots of ionic conductivity of $\text{Ca}_{10-x}\text{Na}_x(\text{PO}_4)_6-x(\text{SO}_4)_x\text{F}_2$ fluorapatite.

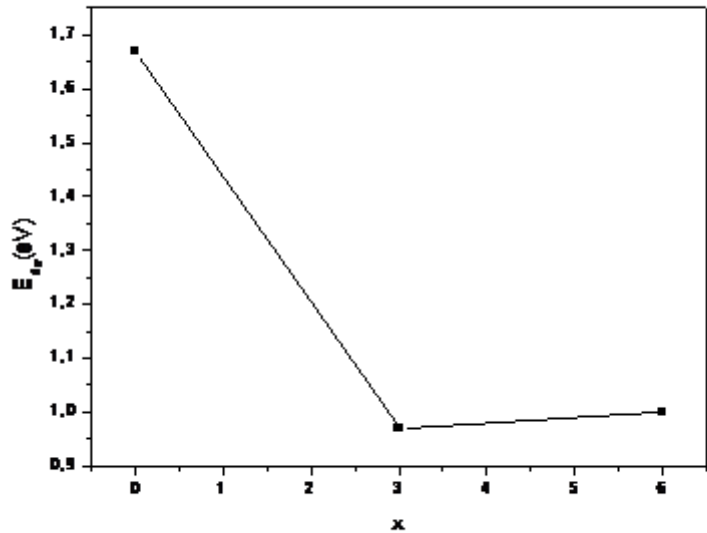


Figure 7

Variation of the activation energy as a function of S content(x) in $\text{Ca}_{10-x}\text{Na}_x(\text{PO}_4)_6-x(\text{SO}_4)_x\text{F}_2$ fluorapatites.

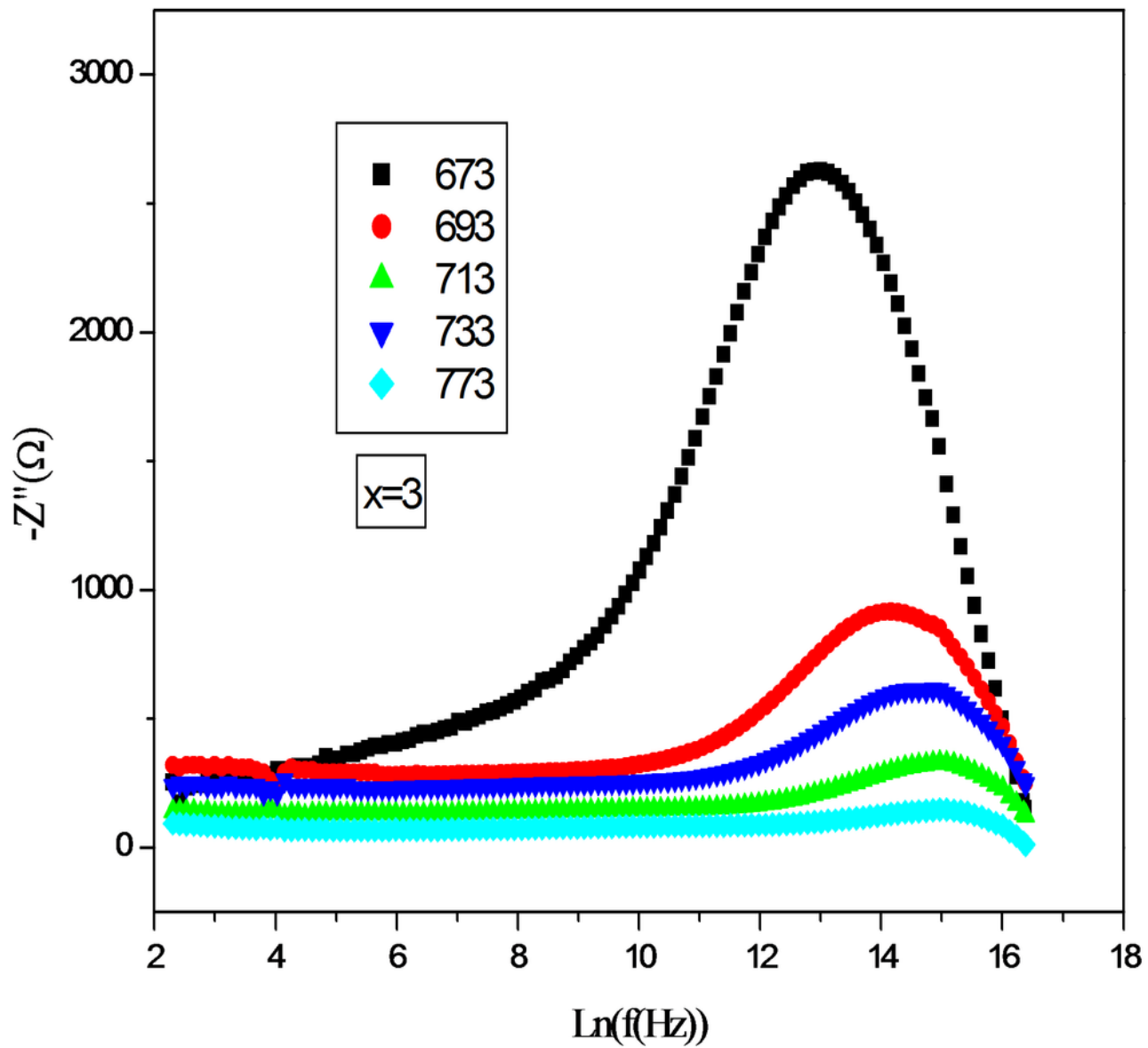


Figure 8

Frequency dependence of ionic conductivity imaginary parts of $\text{Ca}_7\text{Na}_3(\text{PO}_4)_3(\text{SO}_4)_3\text{F}_2$ ($x=3$) fluorapatite.

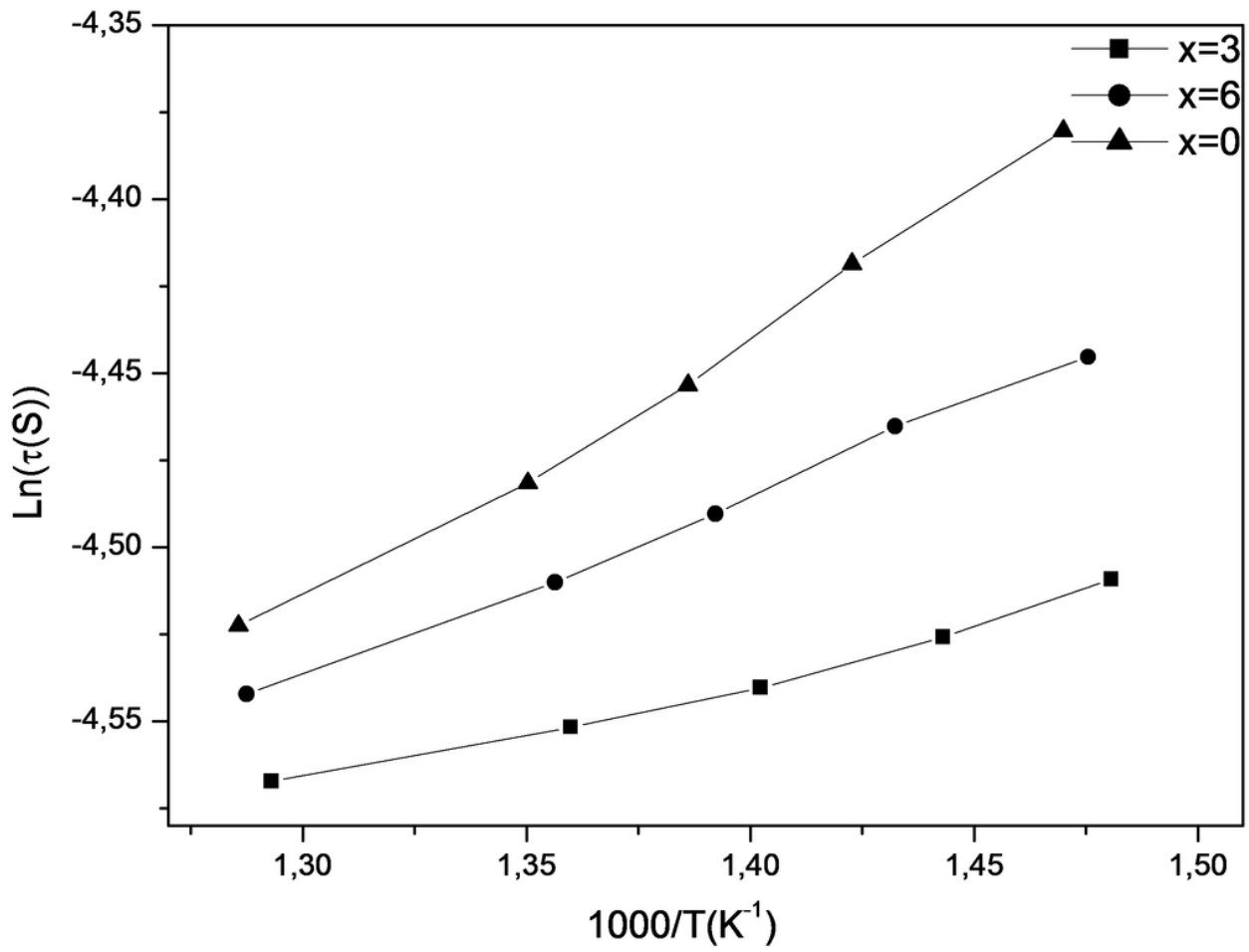


Figure 9

Dependence of relaxation time τ with the inverse of temperature in $\text{Ca}_{10-x}\text{Na}_x(\text{PO}_4)_{6-x}(\text{SO}_4)_x\text{F}_2$ fluorapatite.